

On the origin of the Cold Spot

Kaiki Taro Inoue^{1*}

¹*Department of Science and Engineering, Kinki University, Higashi-Osaka, 577-8502, Japan*

27 July 2021

ABSTRACT

In a concordant Λ Cold Dark Matter (Λ CDM) model, large-angle Cosmic Microwave Background (CMB) temperature anisotropy due to linear perturbations in the local universe is not negligible. We explore a possible role of an underdense region (void) that may cause an anomalous Cold Spot (CS) in the CMB sky. Although the observed anomalous cold region with a surrounding hot ring can be produced by an underdense region surrounded by a massive wall, a decrement in the CMB temperature in the line-of-sight is suppressed because of blueshift of CMB photons that pass the wall. Therefore, undercompensated models give better agreement with the observed data in comparison with overcompensated or compensated models. We find that it is likely that ~ 90 per cent of the CMB fluctuation is generated due to an overdense region surrounded by an underdense region at the last scattering surface, and the remaining ~ 10 per cent is produced due to a single spherical underdense region with a radius $r \sim 6 \times 10^2 h^{-1} \text{Mpc}$ and a density contrast $\delta_m \sim -0.009$ (2σ) at redshift $z \sim 1$ in the line-of-sight to the CS. The probability of having such two aligned structures is ~ 0.7 per cent if the perturbed region at $z \sim 1$ is moderately undercompensated.

Key words: cosmic microwave background – cosmology – large scale structure of the universe.

1 INTRODUCTION

One of the interesting non-Gaussian features found in the cosmic microwave background (CMB) sky is the presence of the Cold Spot (CS) in the Southern hemisphere (Cruz et al. 2005). Although the statistical significance is not significantly high (1.85 per cent) (Cruz et al. 2007), it may be a hint of new physics that is absent in the concordant Λ CDM model. The origin of the temperature decrement may be a time-varying gravitational potential of a supervoid with radius $200 - 300 h^{-1} \text{Mpc}$ in the line-of-sight to the CS (Inoue & Silk 2006, 2007), or that of a cosmological texture at high redshifts $z > 1$ (Cruz et al. 2007). So far, no clear evidence of supervoids in the line-of-sight has been obtained (Rudnick et al. 2007; Bremer et al. 2010; Granett et al. 2010). If such a huge supervoid exists, it will affect various kinds of observables (Das & Spergel 2009; Masina & Notari 2009b,a). Therefore, it can be easily distinguished from other scenarios such as a cosmic texture (Cruz et al. 2007) in the near future.

A key issue is an evaluation of the effect of non-compensation of mass. It has been pointed out that the CS is anomalous because of a hot ring-like structure around it (Zhang & Huterer 2010; Inoue et al. 2010). However, producing a hot ring by a linear or quasi-linear compensated

void is difficult due to the linear integrated Sachs-Wolfe (ISW) effect though such a feature can be realised by non-linear compensated clusters or voids (Tomita & Inoue 2008; Sakai & Inoue 2008; Inoue et al. 2010; Zhan 2011). If one considers a massive wall that overcompensates the low density region inside, such a feature might be easily made even in the case of linear fluctuations. However, we need to estimate the chance of having such structures.

Moreover, in order to explain the entire feature of the CS by a single supervoid, one has to assume an exceptionally huge void, which is difficult to produce in the standard cosmological scenarios (Inoue & Silk 2007). In fact, it is more natural to assume that most of the feature of the CS is produced by fluctuations in the gravitational potential at the last scattering surface (Valkenburg 2012). Therefore, one must take into account various effects such as the ordinary Sachs-Wolfe (OSW) effect (due to spatial fluctuations of the gravitational potential and the temperature) and the Doppler effect due to the bulk velocity of photon-baryon fluid at the last scattering epoch. It is of crucial importance to study the expected value of the percentage of the contribution from an assumed supervoid (or a low density region) to the CS and the most probable redshift in the framework of standard scenarios that predict Gaussian primordial perturbations. Even if the CS has been produced as a fluke, an estimation of a possible contribution from the local structures in the line-of-sight to the CS is important since the

* E-mail: kinoue@phys.kindai.ac.jp

ISW contribution is expected to be maximum in that direction.

The present paper is organised as follows. The linear and the non-linear ISW effects due to a non-compensated void (or cluster) are explored in section 2. The statistical significance of a moderately undercompensated underdense region that will partially explain the CS is discussed in section 3. We conclude the paper in section 4. In the following, unless noted, we assume a concordant Λ CDM cosmology with $(\Omega_{m,0}, \Omega_{\Lambda,0}, \Omega_{b,0}, h, \sigma_8, n) = (0.26, 0.74, 0.044, 0.72, 0.80, 0.96)$, which agrees with the recent CMB and large-scale structure data (Sánchez et al. 2009).

2 MODEL OF NON-COMPENSATED VOID/CLUSTER

In order to investigate temperature variation due to non-compensated underdense or overdense regions, we consider spherically symmetric density fluctuations with a comoving radius r_0 surrounded by a wall at $r_0 < r \leq r_1$. To localise the perturbation, we require that the perturbation is globally compensated. To do so, we introduce a cutoff comoving radius $r_2 \geq r_1$ where the total mass of the perturbation is compensated if integrated over $0 < r < r_2$. In what follows, for simplicity, we only consider top-hat type matter density perturbations for void (cluster) whose linear density contrast is given by

$$\delta^L = \begin{cases} \delta_0^L, & r < r_0 \\ \delta_1^L, & r_0 \leq r < r_1 \\ \delta_2^L, & r_2 \leq r, \end{cases} \quad (1)$$

where δ_0^L, δ_1^L and δ_2^L are constant (Fig. 1). From a condition that the perturbation is local, we have $\delta_0^L r_0^3 + \delta_1^L (r_1^3 - r_0^3) + \delta_2^L (r_2^3 - r_1^3) = 0$. To describe the local mass compensation of the perturbation, we define a parameter ε as

$$\varepsilon \equiv \frac{\delta_0^L r_0^3 + \delta_1^L (r_1^3 - r_0^3)}{|\delta_0^L r_0^3|}. \quad (2)$$

$\varepsilon = 0$ corresponds to a locally compensated case, whereas $\varepsilon > 0$, (or $\varepsilon < 0$) corresponds to a locally overcompensated (undercompensated) case in the region defined by $0 \leq r \leq r_1$ in linear order. Even in the case $\varepsilon = 0$, if $r_1 - r_0 \gtrsim r_0$ and $r_1 = r_2$, we call it a "moderately over(under)compensated" model in the following¹.

In order to incorporate non-linearity of the scalar-type perturbation, we use second order perturbation theory (Tomita & Inoue 2008). In what follows, we assume that the cosmological Newtonian approximation holds for the perturbation that we consider. In other words, we assume that the peculiar velocity is sufficiently smaller than the light velocity, and the size is sufficiently smaller than the present horizon scale. In what follows we only consider growing mode of density perturbation that is adiabatic. The temperature anisotropy due to time-evolving gravitational potential perturbation ψ is given by an integration along with a geodesic of the CMB photon that passes through the potential,

$$\left(\frac{\Delta T}{T}\right) = 2 \int \frac{\partial \psi}{\partial \eta} d\eta, \quad (3)$$

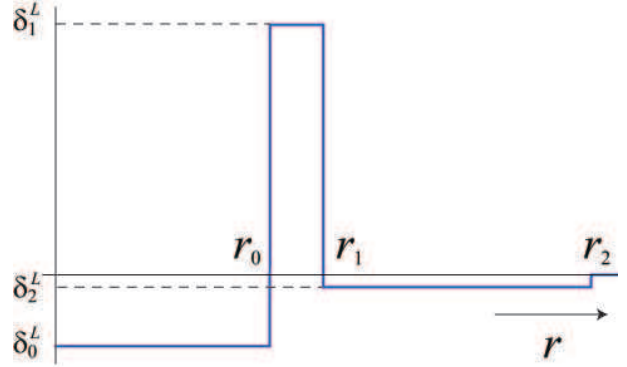


Figure 1. Linear matter density contrast for a top-hat type spherical underdense region.

where η is the conformal time. If the amplitude of the density contrast δ is sufficiently small, the gravitational potential can be expanded as a sum of linear order and second order perturbations $\psi = \psi^L + \frac{1}{2}\psi^S$. Time evolution of the linear perturbation ψ^L is written as a product of a potential function F of comoving coordinates \mathbf{x} and a growing factor $D(\eta)$, which is a function of the scale factor $a(\eta)$ as

$$\begin{aligned} \psi^L(\eta, \mathbf{x}) &= -D(\eta)F(\mathbf{x}) \\ &= \frac{1}{2}\left(1 - \frac{a'}{a}P'\right)F(\mathbf{x}), \end{aligned} \quad (4)$$

where

$$\begin{aligned} P(\eta) &= -\frac{2}{3\Omega_{m0}}a^{-3/2}[\Omega_{m0} + \Omega_{\Lambda0}a^3]^{1/2} \\ &\times \int_0^a da a^{3/2}[\Omega_{m0} + \Omega_{\Lambda0}a^3]^{-1/2} + \frac{2}{3\Omega_{m0}}a. \end{aligned} \quad (5)$$

Here, $\Omega_{m0}, \Omega_{\Lambda0}$ are density parameters of non-relativistic matter and a cosmological constant Λ of the background FRW universe and a prime denotes derivative with respect to the conformal time η . In a similar manner, the second order perturbation ψ^S can be written as

$$\psi^S(\eta, \mathbf{x}) = \xi_1(\eta)F_{,i}(\mathbf{x})F_{,i}(\mathbf{x}) + 100 \xi_2(\eta) \cdot \Psi_0(\mathbf{x}), \quad (6)$$

where $F_{,i}$ is $\partial F / \partial x^i$, and

$$\xi_1 = \frac{1}{4}P\left(1 - \frac{a'}{a}P'\right), \quad (7)$$

$$\xi_2 = \left\{ \frac{1}{21} \frac{a'}{a} \left(P P' - \frac{1}{6} Q' \right) - \frac{1}{18} \left[P + \frac{1}{2} (P')^2 \right] \right\}, \quad (8)$$

and Ψ_0 and $Q(\eta)$ satisfy

$$\Delta \Psi_0 = \frac{9}{200} [F_{,ij} F_{,ij} - (\Delta F)^2], \quad (9)$$

$$Q'' + \frac{2a'}{a} Q' = - \left[P - \frac{5}{2} (P')^2 \right], \quad (10)$$

respectively (Tomita & Inoue 2008). First, we consider effects of linear perturbations. As shown in Fig.2, a hot ring that surrounds a cold spot appears as the wall around an underdense region becomes more massive than a mass deficiency inside since a decay of gravitational potential at an accelerated epoch leads to an increment in the temperature of the CMB photons. Similarly, a cold ring that surrounds a hot spot is produced as an underdense region surrounding an overdense one becomes less massive than a mass that

¹ Alternatively, we may call it "a model with a thick wall".

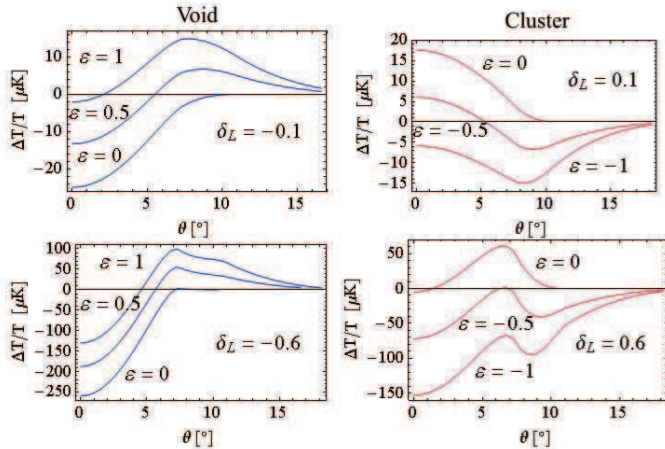


Figure 2. Effect of noncompensation: temperature anisotropies as a function of angular radius θ from the center of the perturbation at redshift $z = 1$ are plotted for voids (left) and clusters (right). The parameters of the mass distribution are set to $(r_0, r_1, r_2) = (0.1H_0^{-1}, 0.15H_0^{-1}, 0.3H_0^{-1})$. Note that the vertical scales of the upper and lower panels are different.

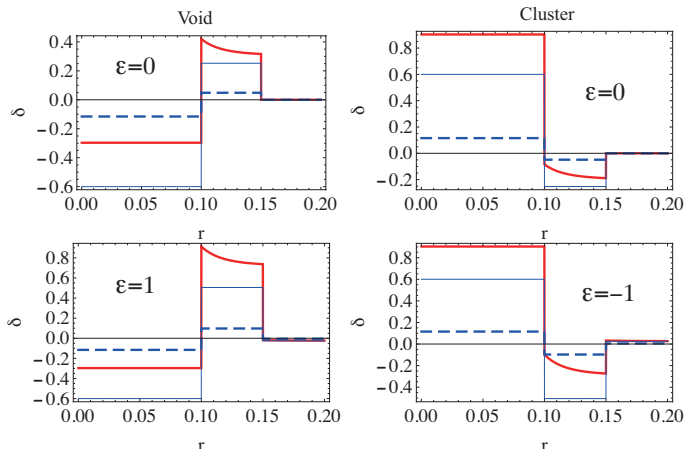


Figure 3. Effect of noncompensation: profiles of mass density contrasts for non-linear density perturbations at $z = 1$ are plotted as thick curves and those for corresponding linear density perturbations are plotted as thin curves ($z = 1$) and dashed curves ($z = 10$) as a function of comoving distance r from the center. The unit of the length is the present Hubble radius H_0^{-1} . The linear density contrasts at the center at $z = 1$ are assumed to be either $\delta_0^L = -0.6$ (left panels) or $\delta_0^L = 0.6$ (right panels). The mass is either locally compensated (upper panels), overcompensated (lower left) or undercompensated (lower right). The parameters of the mass distribution are set to $(r_0, r_1, r_2) = (0.1H_0^{-1}, 0.15H_0^{-1}, 0.3H_0^{-1})$.

compensates the overdense region inside. These behaviors agree with the predicted temperature variation due to the linear ISW effect.

Next, we consider quasi-linear regime. Although the non-linear mass seems to be overcompensated at $r = r_2$ with $\varepsilon = 0$ (see Fig.3), it is actually locally compensated. As shown in Fig.4, the spatial derivative of the potential is not continuous at r_1 . Therefore, it gives a contribution that is proportional to Dirac's delta function $\delta_D(r - r_1)$. Furthermore, if it is smoothed out in the neighbourhood of a

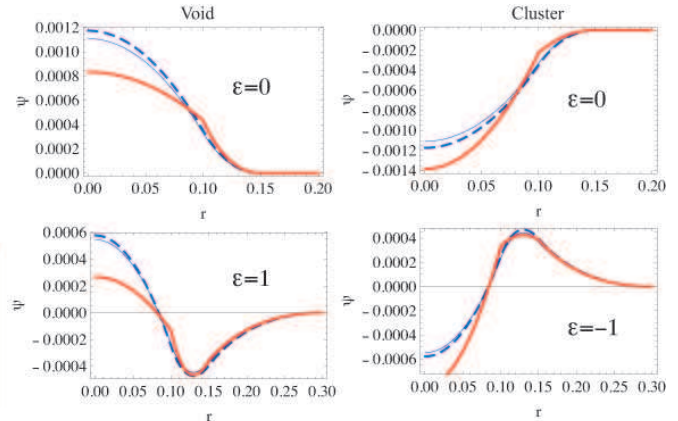


Figure 4. Effect of noncompensation: profiles of gravitational potential for non-linear density perturbations at $z = 1$ are plotted as thick curves and those for corresponding linear density perturbations are plotted as thin curves ($z = 1$) and dashed curves ($z = 10$) as a function of comoving distance r from the center. The parameters are the same as in figure 3.

point $r = r_1$, the gravitational potential becomes concave outward. For this reason, the neighbourhood of $r = r_1$ contributes a negative mass to the density distribution, which leads to a shift of the wall towards the outer (inner) shell $r > r_2$ in the case of a void (cluster). On the other hand, an additional mass due to the second order effect leads to a decrease in the gravitational potential in the inner low density region $0 \leq r < r_1$. Thus, the gravitational potential expands (shrinks) faster than the corresponding linear potential in a void (cluster) in the outer region, but the value of the potential decreases in the inner region as shown in Fig.4². These changes lead to a temperature decrement (increment) in the line-of-sight to the neighbourhood of the center (edge) of the perturbation regardless of the sign of the fluctuation as shown in figure 2.

For non-compensated quasi-linear perturbations, both of the features appear. As shown in figure 2, for overcompensated quasi-linear voids, we would observe a hot ring that surrounds a prominent cold spot. In contrast, for undercompensated quasi-linear clusters, we would see a cold ring that surrounds a cold spot.

Thus it is important to study locally overcompensated (linear/quasi-linear) voids in order to explain the origin of the Cold Spot because it seems to have a hot ring (Inoue et al. 2010).

3 STATISTICAL SIGNIFICANCE

In order to estimate the statistical significance of our model, we use CMB temperature anisotropy ΔT_f that is filtered by

² Interestingly, for quasi-linear clusters, one can see that cancellation between the linear and second order ISW effects can occur and the net temperature anisotropy can vanish near the center if the perturbation is compensated at linear order.

a spherical top-hat type compensating filter defined as

$$W_{th}(\theta; \theta_{in}) = \begin{cases} 1 & (\theta < \theta_{in}) \\ -1 & (\theta_{in} \leq \theta \leq \theta_{out}), \end{cases} \quad (11)$$

where $\theta_{out} = \cos^{-1}(2 \cos \theta_{in} - 1)$.

In the harmonic space, the variance of filtered temperature ΔT_f can be written in terms of the angular power spectrum C_l as

$$\sigma^2 = A(\theta_{in})^{-2} \sum_l C_l W_l^2, \quad (12)$$

where $A(\theta_{in}) = 2\pi(1 - \cos \theta_{in})$ and

$$W_l = \frac{\sqrt{\pi(2l+1)}}{l+1} \left[2 \left(-x_{in} P_l(x_{in}) + P_{l-1}(x_{in}) \right) + x_{out} P_l(x_{out}) - P_{l-1}(x_{out}) \right], \quad (13)$$

$$x_{in} = \cos \theta_{in}, \quad x_{out} = 2x_{in} - 1,$$

where P_l is the Legendre function.

For detail, see appendix of Inoue et al. (2010). Using the WMAP 7-year data, a deviation of $\Delta T_f(\text{CS}) = -72 \mu\text{K}$ is found at smoothing scale $\theta_{in} = 12^\circ$ if centered at the center of the Cold Spot (Inoue et al. 2010). This corresponds to a posteriori significance level of 4σ in the concordant ΛCDM model, since $1\sigma(\theta_{in} = 12^\circ) = 18 \mu\text{K}$ for a single realisation.

Firstly, we assume that a presence of an underdense region in line-of-sight to the Cold Spot contributes $18 \mu\text{K}$ deviation (1σ) of the filtered temperature at smoothing scale $\theta_{in} = 12^\circ$ as an ansatz. The effects of temperature anisotropy due to fluctuations at the last scattering surface or its neighbourhood such as the ordinary Sachs-Wolfe effect, the early integrated Sachs-Wolfe effect and the Doppler effect will be considered in next section.

In order to assess the effect of non-compensation of the surrounding mass, we need to fix shape parameters (r_0, r_1, r_2), degree of overcompensation ε , and redshift z of the center. In terms of comoving distance $d_p(z)$ to the center of the perturbation, the subtending angles of shape parameters are given by $\theta_i = \arctan(r_i/d_p(z))$, $i = 0, 1, 2$. For simplicity, we consider four types of models by fixing the outer boundary r_2 or θ_2 , the next inner boundary r_1 and ε as shown in table 1. Then we calculate the linear density contrast $\delta_0^L(z)$ at the center that will give a filtered temperature anisotropy $18 \mu\text{K}$ as a function of the inner most boundary r_0 and redshift z . In order to assess the probability of a single realisation of such a linear perturbation, we divide the obtained amplitude of the linear density contrast by the standard deviation $\sigma_\delta^L(z)$ of a top-hat type matter density perturbation expected in the concordant ΛCDM model we defined. We use an analytic form of the CDM transfer function (Bardeen et al. 1986) and that of the growth factor for the Friedmann-Robertson-Walker background with dust and a cosmological constant.

As shown in Fig. 5, these 4 types of models give similar values for the best fitting parameters $\theta_0 = 14^\circ - 15^\circ$ and $z \sim 1.0$. Provided that the perturbation is at linear regime, the temperature anisotropy due to the linear ISW effect is proportional to $\delta_0^L r_0^3$ (Inoue & Silk 2006). Therefore, objects at higher redshifts will give larger amplitudes in the temperature anisotropy for a fixed density contrast and a subtending angle in the accelerated epoch. However, if the

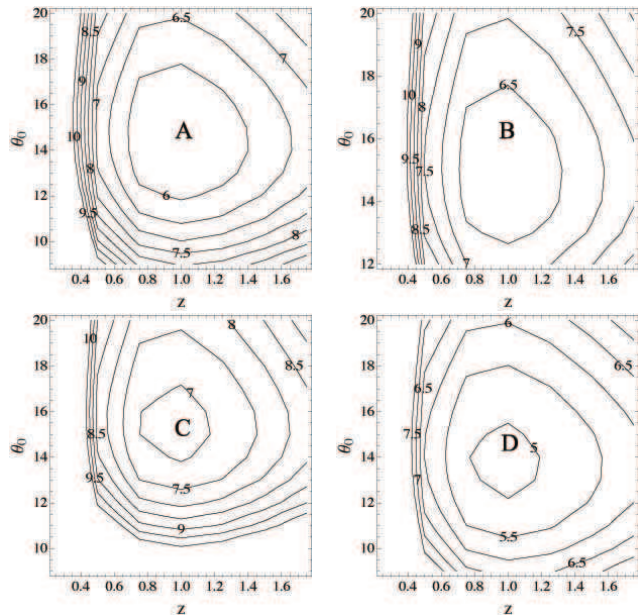


Figure 5. Significance of realisation of a single top-hat type underdense perturbation that will give a signal $\Delta T_f = -18 \mu\text{K}(1\sigma)$ for type A(upper left), type B(upper right), type C(lower left), and type D(lower right). Contour maps of the amplitude of the linear density contrasts δ_0^L at the center in unit of the standard deviation $\sigma_\delta^L(z)$ in a concordant ΛCDM model are plotted as a function of subtending angle of the inner boundary θ_0 and redshift z of the perturbation.

redshift is high enough to decelerate the cosmic expansion, then the linear ISW effect is suppressed. Thus the presence of peak at $z \sim 1$ can be explained as a result of these two different effects. As long as the perturbation is at the linear regime, the place of the peak does not change because the temperature anisotropy is proportional to a density contrast at the center δ_0^L .

Although, a hot ring can be produced by a massive wall ($\varepsilon > 0$) that overcompensates the underdense region inside, overcompensated models (type B and C) are less probable in comparison with a compensated model (type A). For instance, the minimum values (most probable) for type A, B, and C are $5.6\sigma_\delta^L$, $6.1\sigma_\delta^L$, and $6.8\sigma_\delta^L$. For overcompensated models, as we have seen in the previous section, the height of the gravitational potential at the center decreases if the sign of the potential at the wall is negative (Fig. 4) provided that the linear density contrast at the center is fixed. Therefore, redshift effect near the center becomes much weaker and blueshift effect at the surrounding massive wall suppresses further the overall redshifts of the CMB photons that pass through the perturbed region. Thus the linear ISW effect for overcompensated models is suppressed. In contrast, the height of the gravitational potentials for undercompensated models or moderately undercompensated models (such as type D) increases in comparison with the other compensated models with a thin wall (such as type A) since the height of the potential at the center increases. Therefore, the ISW effect is enhanced for undercompensated models.

Second, in order to estimate the statistical significance of our single void (underdense region) model in the concordant ΛCDM model, we need to estimate the CMB

Table 1. Parameters of top-hat type underdense region

Type	ε	r_1	θ_2	category
A	0	$(r_0 + r_2)/2$	30°	compensated
B	0.5	$(r_0 + r_2)/2$	30°	overcompensated
C	1	$(r_0 + r_2)/2$	30°	overcompensated
D	0	r_2	30°	moderately undercompensated

anisotropy due to other effects such as the ordinary Sachs-Wolfe effect due to spatial fluctuation of gravitational potentials and temperature at the last scattering. As we have seen in previous section, the most probable redshift of the underdense region is $z \sim 1$. Therefore, we divide contribution from the ISW effect into two categories, ‘early’ and ‘late’ ones. In what follows, we call the ISW effect due to fluctuations of gravitational potential at $z > 1.5$ the ‘early’ type and at $z < 1.5$ the ‘late’ type, respectively. The origin of the early type ISW effect is a decay of potential due to residual radiation at the time of the last scattering.

For simplicity, we also assume that the late ISW effect mainly comes from a single void (underdense region) in the line-of-sight to the CS. In this calculation, the normalization of the angular power C_l is set by $\sigma_8 = 0.80$. In order to calculate the late type ISW effect, we numerically solve a second-order differential equation for the Newtonian potential Φ on large angular scales. We also use CMB-FAST (Seljak & Zaldarriaga 1996) for calculating the overall small-angle power in which the effect of acoustic oscillation is non-negligible. However, we neglect the effect of reionisation since we are mainly interested in large angular power. Once the angular power C_l of the CMB anisotropy is obtained, the standard deviation $\sigma = \sqrt{(|\Delta T_f|^2)}$ of the filtered temperature anisotropy can be calculated straightforwardly using equation (12). As shown in Fig. 6, the overall amplitude (rms) of the filtered temperature is $\Delta T_f = 18 - 25 \mu\text{K}$ for $\theta_{in} = 4^\circ - 16^\circ$. Because of anti-correlation between fluctuations due to the OSW effect and those due to the early type ISW effect, the overall amplitude at large angular scales is smaller than the sum of the two kinds of amplitudes. In contrast, correlation between fluctuations due to the OSW effect and those due to the late type ISW effect is small if the corresponding size of the fluctuations are sufficiently smaller than the present horizon scale. Contribution from the late type ISW effect to the overall amplitude is about 25 per cent for $\theta_{in} = 12^\circ$. On smaller angular scales, the contribution becomes smaller. For instance, we find that contribution from fluctuations at redshift $0.45 < z < 0.75$ is just $\sim 1 \mu\text{K}$. This result is consistent with the previous calculation for superstructures in the SDSS-LRG catalog (Inoue et al. 2010).

Finally, in order to calculate the statistical significance of a single void (underdense region) in the line-of-sight to the CS, we assume that it is described by a moderately undercompensated top-hat type linear perturbation with $\theta_1 = \theta_2 = 30$ degree (type D). We calculate the innermost radius of the perturbation r_0 that is most probable for a given redshift z of the center for a given amplitude of the filtered temperature $\Delta T_f(\text{void})$ for $\theta_{in} = 12^\circ$ as shown in the previous section. Then for each spherical shell with comoving radius $d_p(z) - r_0 < r < d_p(z) + r_0$, the probability $P_{\text{void}}(\Delta T_f(\text{void}); z)$ of finding such a fluctuation

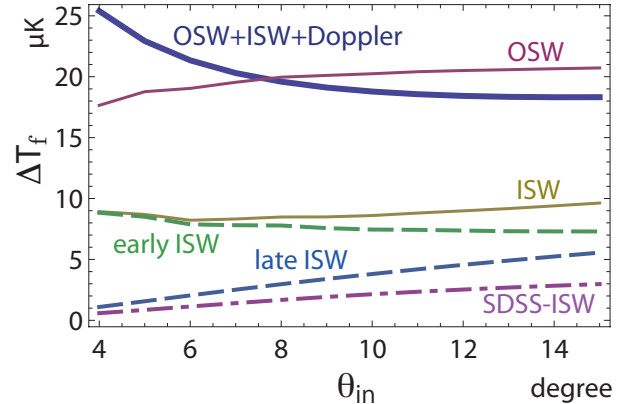


Figure 6. Root-mean-square values of the amplitude of the filtered CMB temperature anisotropy in a concordant ΛCDM model due to the Doppler effects (blue thick curve), the OSW effect (purple thin curve), the ISW effect (green thin curve), the early type ISW effect (green dashed curve), the late type ISW effect (blue dashed curve), and the ISW effect from a region at $0.45 < z < 0.75$ (purple dot-dashed curve).

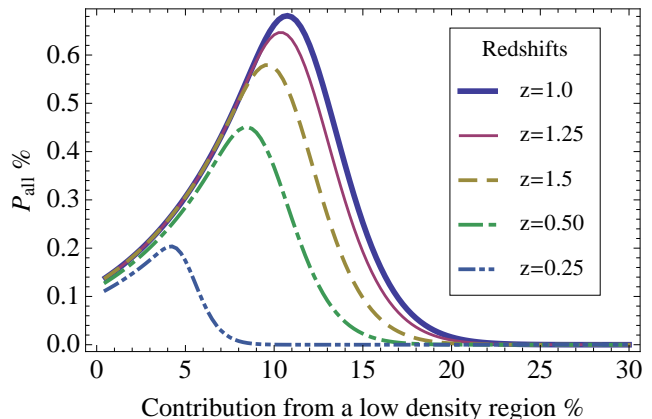


Figure 7. Overall probabilities as a function of contribution from a low density region (void) for various redshifts.

is calculated based on linear perturbation theory assuming the CDM power spectrum (Bardeen et al. 1986). We approximate the probability distribution of the filtered temperature by a Gaussian distribution since the filtered temperature is described as a sum of a number of independent modes in the harmonic space. The number of independent perturbed low density region for a given angular scale $r_0/d_p(z)$ is approximated as $N \sim d_p(z)^2/(2r_0^2)$.

Then the probability distribution function of the filtered temperature fluctuation due to a single void is $P_{\text{void}} = 1 - F(x)^N$ where $F(x)$ is the cumulative distribution for the Gaussian distribution $g(x) = 2/\sqrt{2\pi} \exp(-x^2/2)$ and $x = \Delta T_f(\text{void})/\sqrt{\langle(\Delta T_f(\text{void}))^2\rangle}$. The probability distribution function P_{LSS} of finding filtered temperature anisotropy $|\Delta T_f(\text{LSS})| = (72 - |\Delta T_f(\text{void})|)\mu\text{K}$ for $\theta_{in} = 12^\circ$ due to the OSW, early type ISW and Doppler effects can be calculated as $P_{\text{LSS}} = g(y)$, where $y = \Delta T_f(\text{LSS})/\sqrt{\langle(\Delta T_f(\text{LSS}))^2\rangle}$.

Then the overall probability distribution function of finding such configuration is given by $P_{\text{all}} = P_{\text{LSS}}P_{\text{void}}$. Note that we have neglected any contributions due to fluctuations at redshifts $z < 1.5$ except for the assumed low density region (void). This is verified if the center of the low density region is at $z \sim 1$ because the late type ISW effect is maximum at this redshift for the assumed angular scale $\theta_0 \sim 14^\circ$ as we have seen in the previous section.

In Fig.7, the overall probability $P_{\text{all}}(\geq |\Delta T_f(\text{CS})| = 72\mu\text{K})$ as a function of percentage of contribution from an assumed low density region (void), $\Delta T_f(\text{void})/72\mu\text{K} \times 100$, is plotted for various redshifts of the region. We find that the most probable values of redshift and contribution to the filtered temperature from a low density region are $z = 1.0$ and 11 per cent, respectively. The remaining 89 per cent of temperature anisotropy is produced by an overdense and surrounding underdense region at the last scattering surface in the line-of-sight to the CS. The maximum value of the overall probability of our model is $P_{\text{all}} = 0.68$ per cent. This result indicates that a contribution from the late type ISW effect due to an underdense region in the line-of-sight to the CS is not completely negligible. Indeed, it turns out that the possibility of having such a contribution is maximally 7 times larger in comparison with the case without a single underdense region in the line-of-sight to the CS.

The most probable parameters of our model is summarized in table 3. The temperature profile due to the most probable underdense region is plotted in Fig.8. The expected temperature decrement in the direction to the center is $-21\mu\text{K}$. The density contrast is $\delta_0^L = -0.0085$ corresponding to 2.1σ or a probability of 1 in 10 for a single realisation of negative density fluctuation at $z = 1$. Therefore, it is not rare to have such an underdense region. As we can see from Fig.8, a hot-ring like structure around the cold region cannot be attributed to the low density region at $z \sim 1$. If it is attributed to the OSW effect, we need to assume a potential hill at the last scattering surface. Therefore, it is most likely that a low density region surrounding a high density region resides at the last scattering surface.

4 CONCLUSION

We have explored a possible role of an underdense region (void) that may cause an anomalous Cold Spot (CS) in the Cosmic Microwave Background (CMB) sky located at the southern Galactic hemisphere. Although we have found that the observed cold spot with a hot ring can be reconstructed by an underdense region surrounded by a massive wall that overcompensates the mass deficiency inside, the CMB temperature decrement in the line-of-sight to the center due to the linear integrated Sachs-Wolfe (ISW) effect is suppressed because of blueshift of CMB photons at the wall surrounding

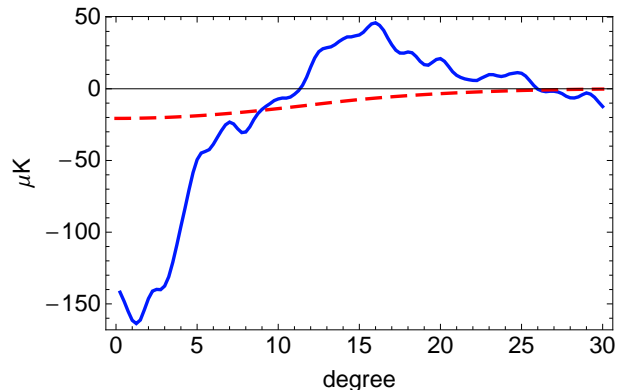


Figure 8. Temperature anisotropy due to a decaying potential of a single low density region (model D) (red dashed curve) and the observed Cold Spot (WMAP7) smoothed in azimuthal direction (blue full curve). For detail, see Inoue et al. (2010). The horizontal line represents the angular radius from the center of the CS. The parameters of the low density region are given in table 2.

an underdense region. Therefore, undercompensated models give better agreement with the observed data in comparison with overcompensated or compensated models. It is likely that ~ 90 per cent of the CMB fluctuation is generated at an overdense region surrounded by an underdense region at the last scattering surface, and the remaining ~ 10 per cent is produced due to a single underdense region that is moderately undercompensated with radius $r \sim 6 \times 10^2 h^{-1}\text{Mpc}$ and a density contrast $\delta_m \sim -0.009$ (corresponding to $\sim 2\sigma$ for a single realisation) at redshift $z \sim 1$. The probability of having such aligned structures is ~ 0.7 per cent if the underdense region is moderately undercompensated. The temperature decrement due to the ISW effect is expected to be $\sim -20\mu\text{K}$ in the line-of-sight to the center. It should be emphasised that the chance of having such an underdense region is 7 times larger in comparison with the case without any underdense regions in the line-of-sight to the CS in the concordant ΛCDM model with Gaussian primordial perturbations. If such a linear underdense region does not reside at redshift $z \sim 1$, then either an abnormally large quasi-linear void at low redshift $z < 0.3$, or non-Gaussian density fluctuations at $z \gg 1$ is necessary for explaining the origin of the CS. Therefore, it is very important to probe the density profile in the line-of-sight to the CS at redshifts $0.3 < z < 2$ subtending an angular radius $\theta > 15^\circ$ in future survey. Ongoing projects such as LSST (Ivezic 2008) and SKA (Blake et al. 2004) might be helpful for this purpose.

We have not considered effects of non-sphericity of the density profile and chance alignments between other large scale structures in the line-of-sight, which are considered to be minor effects. However, it will certainly improve the accuracy of model prediction if we can take into account these effects as well. These effects will be investigated in our future work.

5 ACKNOWLEDGMENTS

I thank K.Tomita, N.Sakai, J. Silk and anonymous referee for useful comments. Some of the results presented here have been derived using the Healpix package (Górski et al. 2005).

Table 2. The most probable parameters for the type D underdense region

z	δ_0^L	θ_0	θ_1	r_0	$\Delta T_f(\text{void})$	$P_{\text{all}}(\%)$
1.0	-0.0085	14°	30°	$570h^{-1}\text{Mpc}$	$7.7\mu\text{K}$	0.68

I acknowledge the use of the Legacy Archive for Microwave Background Data Analysis (LAMBDA)(Lambda website). Support for LAMBDA is provided by the NASA Office of Space Science. This work is in part supported by a Grant-in-Aid for Young Scientists (B)(20740146) of the MEXT in Japan.

Zhang R., Huterer D., 2010, *Astroparticle Physics*, 33, 69

REFERENCES

- Bardeen J. M., Bond J. R., Kaiser N., Szalay A. S., 1986, *The Astrophysical Journal*, 304, 15
- Blake C. A., Abdalla F. B., Bridle S. L., Rawlings S., 2004, *New Astronomy Review*, 48, 1063
- Bremer M. N., Silk J., Davies L. J. M., Lehnert M. D., 2010, *Monthly Notices of the Royal Astronomical Society*, 404, L69
- Cruz M., Cayón L., Martínez-González E., Vielva P., Jin J., 2007a, *The Astrophysical Journal*, 655, 11
- Cruz M., Martínez-González E., Vielva P., Cayón L., 2005, *Monthly Notices of the Royal Astronomical Society*, 356, 29
- Cruz M., Turok N., Vielva P., Martínez-González E., Hobson M., 2007b, *Science*, 318, 1612
- Das S., Spergel D. N., 2009, *Physical Review D*, 79, 43007
- Górski K. M., Hivon E., Banday A. J., Wandelt B. D., Hansen F. K., Reinecke M., Bartelmann M., 2005, *The Astrophysical Journal*, 622, 759
- Granett B. R., Szapudi I., Neyrinck M. C., 2010, *The Astrophysical Journal*, 714, 825
- Inoue K. T., Sakai N., Tomita K., 2010, *The Astrophysical Journal*, 724, 12
- Inoue K. T., Silk J., 2006, *The Astrophysical Journal*, 648, 23
- Inoue K. T., Silk J., 2007, *The Astrophysical Journal*, 664, 650
- Ivezic Z. e. a., 2008, e-print:arXiv0805.2366
- Masina I., Notari A., 2009a, *Journal of Cosmology and Astro-Particle Physics*, 07, 035
- Masina I., Notari A., 2009b, *Journal of Cosmology and Astro-Particle Physics*, 02, 019
- Rudnick L., Brown S., Williams L. R., 2007, *The Astrophysical Journal*, 671, 40
- Sakai N., Inoue K. T., 2008, *Physical Review D*, 78, 63510
- Sánchez A. G., Crocce M., Cabré A., Baugh C. M., Gaztañaga E., 2009, *Monthly Notices of the Royal Astronomical Society*, 400, 1643
- Seljak U., Zaldarriaga M., 1996, *The Astrophysical Journal*, 469, 437
- Tomita K., Inoue K. T., 2008, *Physical Review D*, 77, 103522
- Valkenburg W., 2012, *Journal of Cosmology and Astroparticle Physics*, 01, 047
- Zhan H., 2011, *The Astrophysical Journal*, 740, 26